Static and dynamical properties of the spin-$\frac{5}{2}$ nearly ideal triangular lattice antiferromagnet Ba$_3$MnSb$_2$O$_9$

Mingfang Shu [1,2,*], Weicen Dong, [1,2,*] Jinlong Jiao [1,2], Jiangtao Wu,[1,2] Gaoting Lin,[1,2] Yoshitomo Kamiya [1,2,†]
Tao Hong,[3] Huibo Cao [3], Masaaki Matsuda [3], Wei Tian,[3] Songxue Chi [3], G. Ehlers,[3] Zhongwen Ouyang,[4]
Hongwei Chen,[5,7] Youming Zou,[5] Zhe Qu [5], Qing Huang,[6,§] Haidong Zhou,[6] and Jie Ma [1,2,4,‡]

[1]*Key Laboratory of Artificial Structures and Quantum Control, School of Physics and Astronomy,*
Shanghai Jiao Tong University, Shanghai 200240, China
[2]*Collaborative Innovation Center of Advanced Microstructures, Nanjing University, Nanjing 210093, Jiangsu, China*
[3]*Neutron Scattering Division, Oak Ridge National Laboratory, Oak Ridge, Tennessee 37831, USA*
[4]*Wuhan National High Magnetic Field Center, Huazhong University of Science and Technology,*
Wuhan 430074, People's Republic of China
[5]*Anhui Key Laboratory of Condensed Matter Physics at Extreme Conditions, High Magnetic Field Laboratory,*
Hefei Institutes of Physical Sciences, Chinese Academy of Sciences, Hefei, Anhui 230031, China
[6]*Department of Physics and Astronomy, University of Tennessee, Knoxville, Tennessee 37996, USA*
[7]*College of Materials Science and Chemistry, China Jiliang University, Hangzhou 310018, China*

We study the ground state and spin excitations in Ba$_3$MnSb$_2$O$_9$, an easy-plane $S = 5/2$ triangular lattice antiferromagnet. By combining single-crystal neutron scattering, electric spin resonance (ESR), and spin wave calculations, we determine the frustrated quasi-two-dimensional spin Hamiltonian parameters describing the material. While the material has a slight monoclinic structural distortion, which could allow for isosceles-triangular exchanges and biaxial anisotropy by symmetry, we observe no deviation from the behavior expected for spin waves in the in-plane 120° state. Even the easy-plane anisotropy is so small that it can only be detected by ESR in our study. In conjunction with the quasi-two-dimensionality, our study establishes that Ba$_3$MnSb$_2$O$_9$ is a nearly ideal triangular lattice antiferromagnet with the quasiclassical spin $S = 5/2$, which suggests that it has the potential for an experimental study of Z- or Z_2-vortex excitations.

I. INTRODUCTION

In geometrically frustrated systems, the complicated interplay between electrons, lattice, spins and orbitals can lead to macroscopic degeneracy in the low-energy states. Qualitatively new states of matter can emerge from such nontrivial state manifold, which has been the subject that attracts huge experimental and theoretical interests over the past decades [1–6]. The ground state manifold can be more complex than unfrustrated systems, giving rise to a possibility of hosting unconventional topological defects and associated topological transitions [7].

The two-dimensional (2D) triangular-lattice antiferromagnetic Heisenberg model (TLAHM) is one of the simplest prototypical models that exhibit typical 2D properties at low temperatures [8,9]. For small spin S, the combination of reduced dimensionality, geometric frustration, and the enhanced quantum fluctuations can stabilize exotic quantum states [10,11]. For example, the transition from the non-collinear 120° state to the up-up-down state is a quantum order by disorder phenomenon in which the state is selected by quantum fluctuations from a degenerate manifold in a magnetic field [12]. Even the semiclassical 120° state has profound consequences of strong quantum fluctuation in the magnon spectrum: the magnon dispersion can display strong band renormalization and the excitation continuum with anomalously large spectral weights due to the magnon-magnon interaction [13]. Although these established quantum effects may be observed only for relatively small spins, such as $S = 1/2$ or $S = 1$ [14–16], several recent experimental studies reported similar anomalous behaviors in presumably more classical spin systems with relatively large S, such as a rotonlike minimum, a flat mode, and magnon linewidth broadening in LuMnO$_3$ ($S = 2$) [17]. Meanwhile, these effects are mostly suppressed in the isostructual material HoMnO$_3$ ($S = 2$) [18]. Except for the possible enhanced magnon damping effect due to the non-collinear nature of the magnetic order [13,19,20], the precise mechanism of such pseudo-quantum behaviors in relatively large spin systems is unclear and it is imperative to find new materials and perform further investigation using high-quality single-crystal samples.

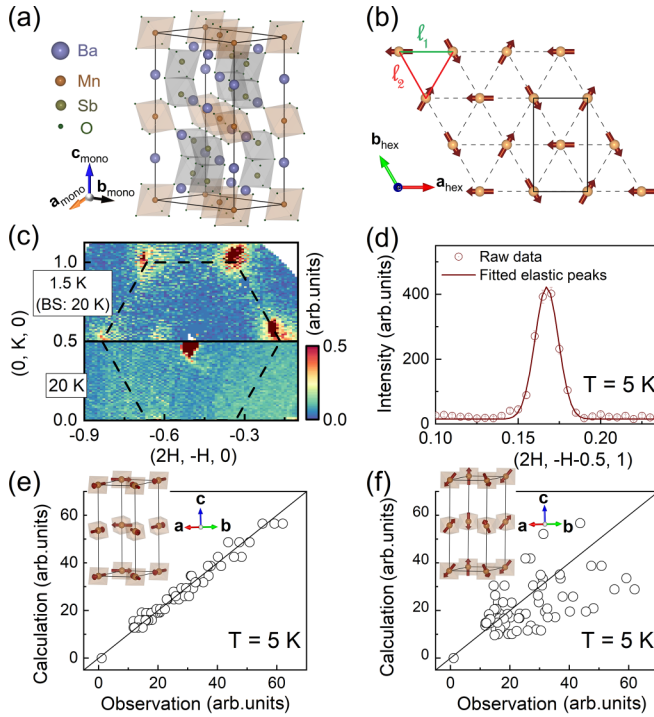Triple-perovskite materials Ba$_3$MM'$_2$O$_9$ ($M =$ Co, Ni, Mn, $M' =$ Sb, Nb) comprise triangular lattice layers of magnetic

FIG. 1. (a) Schematic crystal structure of $Ba_3MnSb_2O_9$. (b) Triangular lattice of Mn^{2+} ions in the *ab* plane. (c) Elastic magnetic scattering in the *HK* plane at 20 K (bottom) and the data at $T = 1.5$ K with the background subtraction (BS) of the 20 K data (top). (d) The elastic magnetic scattering along $(2H, -H - 0.5, 1)$ and the fitting result. [(e) and (f)] Comparison between the observed magnetic Bragg peak intensities at 5 K on the HB-3A DEMAND and the simulated ones based on the $120°$ structure in the (e) *ab* and (f) *ac* planes, respectively, with the insets showing the schematic magnetic structures. The solid lines are guides to the eye.

M ions separated by nonmagnetic buffer layers of M' ions and Ba ions, thus providing an ideal platform for exploring exotic magnetism of quasi-2D TLAHM [21]. $Ba_3CoSb_2O_9$ ($S = 1/2$) is known for the up-up-down state stabilized by quantum order by disorder [14,22–27] and the anomalous zero-field magnetic excitations [28–34]. The triple-perovskite family also includes interesting high-spin materials, such as the multiferroic material $Ba_3MnNb_2O_9$ ($S = 5/2$) [35]. The diversity of the triple-perovskite family allows for detailed comparative studies between materials with different *S*, and different lattice symmetries, and various degrees of quasi-two-dimensionality [36–38]. However, previous experimental studies on the large-*S* triple-perovskite family have been largely limited to polycrystalline samples, and studies using high-quality single-crystal samples are desired for more detailed assessments of their physical properties.

In this paper, we report the synthesis and the characterization using single crystal of the spin-5/2 quasi-2D TLAHM material $Ba_3MnSb_2O_9$ (Fig. 1). $Ba_3MnSb_2O_9$ consists of corner-sharing MnO_6 octahedra and face-sharing Sb_2O_9 bi-octahedra. The interlayer exchange interaction is expected to be much smaller than the intralayer exchange interaction in $Ba_3MnSb_2O_9$, similar to $Ba_3CoSb_2O_9$. Our detailed elastic and inelastic neutron scattering (INS) measurements confirm that the material has the $120°$ magnetic order in the *ab* plane

in zero field, in agreement with the previous result of the polycrystalline sample [21]. We find that the INS data are well described by the quasi-2D TLAHM for $S = 5/2$ with nearly isotropic interactions, where the interlayer exchange interaction J_c is about 5% of the intralayer nearest-neighbor exchange interaction J_1.

The crystal structure of $Ba_3MnSb_2O_9$ is monoclinic [space group C2/c (No. 15)], rather than hexagonal. Compared with $Ba_3CoSb_2O_9$, the replacement of Co^{2+} ions (ionic radius: 0.745 Å) by Mn^{2+} ions with the larger ionic radius (0.830 Å for the high-spin state) induces a lattice distortion, causing one edge of the triangular l_1 to be 5.881 Å and the other two edges l_2 to be 5.877 Å, Fig. 1(b) [21,39]. The spin Hamiltonian for such a system might have isosceles-triangular exchanges and biaxial anisotropy $D_x(S^x)^2 + D_z(S^z)^2$. However, our study confirms no deviation from the behavior of the in-plane $120°$ state expected in an equilateral TLAHM system. As expected for Mn^{2+} ($3d^5$), even the magnitude of the easy-plane anisotropy D_z is very small (about 0.3% of J_1), which is detected in ESR measurements instead of INS experiments. Therefore, in conjunction with the quasi-two-dimensionality, $Ba_3MnSb_2O_9$ is suggested to be a nearly ideal realization of the TLAHM with the quasiclassical spin $S = 5/2$.

For such a system, the nature of topological excitations and the possibility of having a Kosterlitz-Thouless like transition have been a long-debated subject [7,40–46]. On one hand, topological excitations in the $120°$ ordered state are relatively unconventional Z_2 vortices in an ideal isotropic TLAHM with SU(2) symmetry, because the SO(3) order parameter manifold is isomorphic to the three-dimensional real projective space RP^3 and $\pi_1(RP^3) = Z_2$ [7]. On the other hand, when the spin symmetry is reduced to $Z_2 \times U(1)$ by uniaxial anisotropy, topological excitations are Z vortices ($\pi_1(S^1) = Z$, where the circle S^1 corresponds to the manifold of the in-plane rotation), i.e., conventional vortices with integer charge, in addition to chiral domain walls. In such context, the close proximity of $Ba_3MnSb_2O_9$ to the ideal isotropic TLAHM due to the very small anisotropy makes it a promising material for the study Z- or Z_2-vortex excitations experimentally [7,40–46].

II. EXPERIMENTS

$Ba_3MnSb_2O_9$ single crystal was synthesized by using the floating zone method and a commercial physical property measurement system (PPMS, Quantum Design) was applied to obtain the specific-heat, DC magnetic susceptibility, and DC magnetization. Elastic neutron scattering data were collected at 5 K with the wavelength of 1.54 Å by the Four-Circle Diffractometer (HB-3A) at the High Flux Isotope Reactor (HFIR), Oak Ridge National Laboratory (ORNL) [47] and the structure refinements were performed using FULLPROF [48]. The INS experiments were carried out with the use of both Cold Neutron Triple-Axis Spectrometer (CG-4C) at HFIR and the high-resolution time-of-flight spectrometer Cold Neutron Chopper Spectrometer (CNCS) at the spallation neutron source (SNS), ORNL. The final neutron energy of CG-4C was fixed as 5 meV with an instrumental energy resolution of about 0.15 meV and the incident neutron energy of CNCS was fixed to 3 meV with an instrumental resolution of 0.07 meV, respectively. Our INS measurements were performed at $T =$
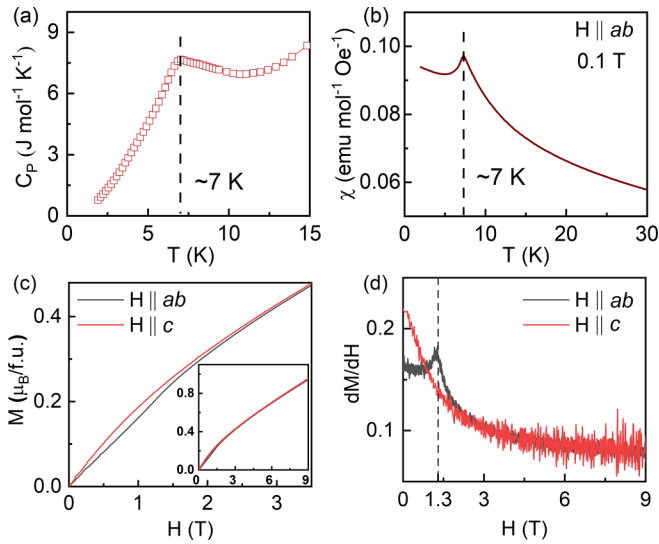
FIG. 2. [(a) and (b)] Temperature-dependent (a) specific heat and (b) DC magnetic susceptibility of $Ba_3MnSb_2O_9$. (c) DC magnetization at 2 K for $\mathbf{H} \parallel ab$ and $\mathbf{H} \parallel c$ with the inset showing the full curves up to 9 T. (d) dM/dH, where the vertical dashed line indicates a field-induced transition near 1.3 T for $\mathbf{H} \parallel ab$.

1.5 and 20 K. The entire four-dimensional set of the CNCS data was analyzed using the software package DAVE. Finally, the pulsed-field ESR data were collected at Wuhan National Pulsed High Magnetic Field Center using a pulsed magnetic field of up to 20 T.

A. Thermodynamic measurements

The specific heat and the DC susceptibility for $Ba_3MnSb_2O_9$ indicate an antiferromagnetic transition at around 7 K, Figs. 2(a) and 2(b), which is slightly lower than the reported one for polycrystalline samples ($T_N = 10.2$ K) [49]. Moreover, the shape of the specific heat peak shows a more rounded feature, while the previous polycrystalline data exhibits λ-type anomaly [21,49]. The isothermal DC magnetization at $T = 2$ K is shown in Fig. 2(c). The magnetization does not saturate in the investigated field region ($H_{sat} = 49$ T is reported in the literature [50]). A closer examination confirms that the magnetization process behaves slightly differently depending on the direction of the magnetic field in the range of 0–3 T. For $\mathbf{H} \parallel ab$, a small peak is observed in dM/dH at around 1.3 T [Fig. 2(d)]. An inspection of the model discussed later suggests that this may correspond to a field-induced spin-flop transition.

B. Neutron scattering results

The elastic scattering map in the $HK0$ plane at 1.5 K with the subtraction of the data at 20 K is presented in Fig. 1(c). Hereafter, since the monoclinic distortion of the perovskite structure is very small ($|\mathbf{a}_{mono}| \approx |\mathbf{a}_{hex}|$, $|\mathbf{b}_{mono}| \approx \sqrt{3}|\mathbf{a}_{hex}|$, $|\mathbf{c}_{mono}| \approx |\mathbf{c}_{hex}|$, and $\beta_{mono} \approx 90.3°$), we adopt a hexagonal unit cell. The elastic scattering map reveals the magnetic Bragg peaks at K points, indicating a magnetic order [Fig. 1(d)]. To determine the magnetic structure of $Ba_3MnSb_2O_9$, the neutron diffraction data are

refined using FULLPROF. According to the Rietveld analysis, there is slight Sb-deficiency ($\approx 4\%$) in this compund owing to the low melting point of Sb. Depending on easy-plane or easy-axis anisotropy, the 120° structure expected for the TLAHM can be in the plane parallel or perpendicular to the ab plane, respectively [51]. Although the same set of magnetic Bragg peaks are generated, a close examination of the scattering intensity distribution can distinguish these two cases. The 120° structure in the ab plane [Fig. 1(e)] is more consistent with the experiment than one in the ac plane [Fig. 1(f)], suggesting easy-plane anisotropy, and the ordered magnetic moment is $4.9 \mu_B$. The monoclinic crystal distortion may allow for isosceles-triangular exchanges [39] and biaxial anisotropy [50], possibly leading to small deviations from the ideal 120° structure, such as long-wavelength incommensuration or a commensurate deformation within the three-sublattice structure. However, our experiments detect no deviation from the in-plane 120° state, e.g., the fitting result of the ordering wave vector is $\mathbf{Q} = (0.334(7), -0.667(3), 1)$. The ordered moments in even and odd layers are in a staggered orientation along the c axis, which indicates that the interlayer exchange interaction J_c is antiferromagnetic. Thus, experimentally, the magnetic structure of the ground state is consistent with the 120° spin structure in the ab plane with the magnetic propagation vector $(1/3, 1/3, 1)$, similar to $Ba_3CoSb_2O_9$ [52].

To investigate the spin dynamics in $Ba_3MnSb_2O_9$, INS scattering data were collected at 1.5 K. The energy-momentum map of the scattering intensity along the high-symmetry directions in the reciprocal plane $L = 0$ is shown in Fig. 3(a). The overall bandwidth of the single-magnon dispersion is around 2.0 meV. The largest intensity of the inelastic scattering is found near the magnetic Bragg wave vectors $K_{1,2}$. The L dependence of the scattering intensity along the c axis is shown in Figs. 3(b) and 3(c) for $\mathbf{q} = (-1, 1/2, L)$ and $(1/3, -2/3, L)$, respectively. Although the dispersion along $(-1, 1/2, L)$ is nearly flat, the magnon excitation for $(1/3, -2/3, L)$ is clearly dispersive, pointing to a small but nonnegligible antiferromagnetic interlayer exchange interaction J_c. In Fig. 4, we summarize the line shapes of the scattering intensity at selected momenta as well as the peak positions estimated by using Gaussian fitting, which will be used in our theoretical analysis (see Sec. III).

The evolution of the scattering intensity with increasing energy is highlighted in constant-energy slices in Figs. 3(g)–3(i). The constant-energy profile at 0.6 meV displays sharp magnon excitations at around the K points. With increasing energy, the position of the strong scattering intensity shifts towards M_2, while the intensity at the K_2 point decreases. For the larger energy 1.25 meV, we find that the intensity pattern forms triangular shapes around the Brillouin zone corners. In addition, a nearly flat magnon excitation is observed along the M_2M_3 line. Both features are known to be characteristics of the spin-wave dispersion in the TLAHM [33,53]. At a higher energy, $E = 2$ meV, the spin excitations form hexagonal ring-like patterns around the Γ point.

C. ESR results

To obtain the magnetic excitation at the magnetic zone center $\mathbf{q} = (0, 0, 0)$, the electron spin resonance (ESR)
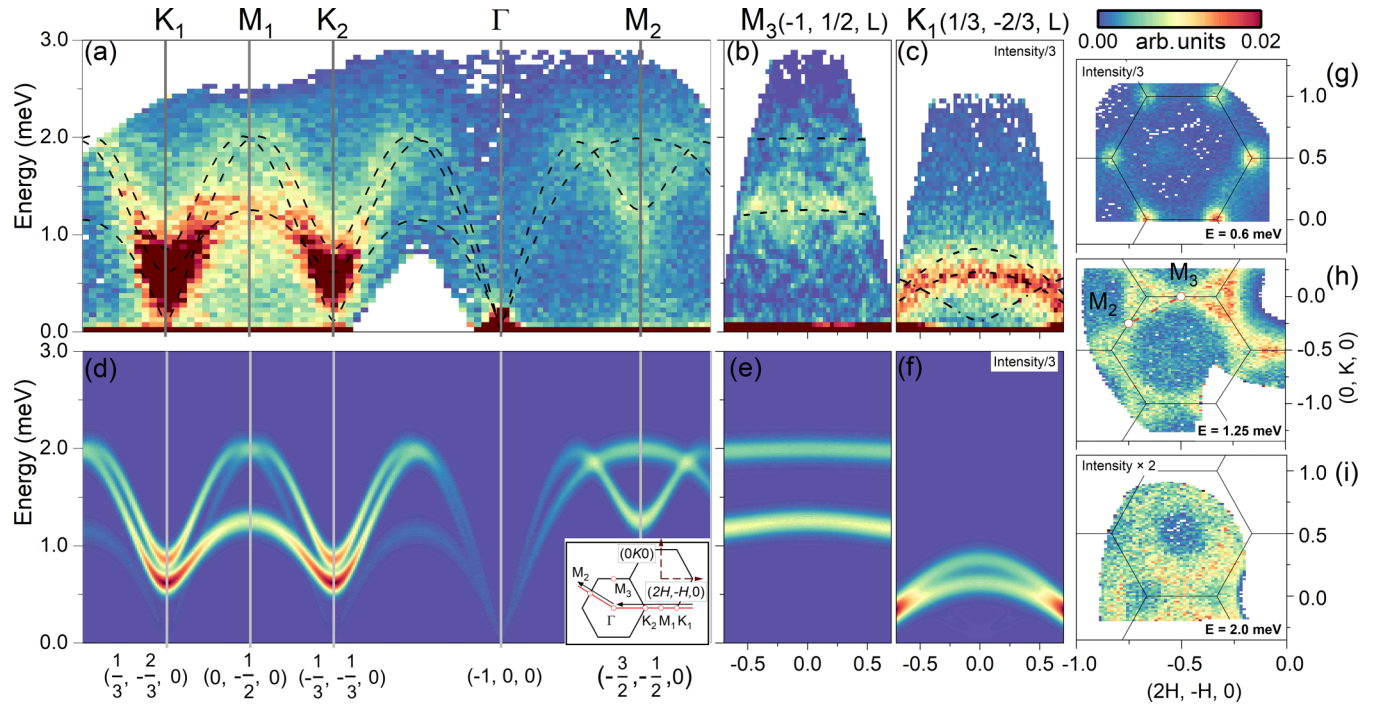
FIG. 3. Excitation spectra of $Ba_3MnSb_2O_9$ measured at $T = 1.5$ K (BS: 20K). [(a)–(c)] Energy-momentum maps of the scattering intensity along (a) the in-plane high-symmetry directions at $L = 0$ [see the inset in (d)], (b) $\mathbf{q} = (-1, 1/2, L)$, and (c) $(1/3, -2/3, L)$. The dashed lines are the fitted dispersion relations using the LSW theory. (d)–(f) Intensity plots of the dynamical structure factor calculated by the LSW theory along the same symmetry lines in (a)–(c). The instrumental energy resolution (0.07 meV) is used for the Gaussian broadening factor. [(g)–(i)] INS intensity maps as a function of the momentum in the HK plane ($L = 0$) at (g) 0.6, (h) 1.25, and (i) 2.0 meV.

spectra, $f(H)$, were measured at 2 K, as shown in Fig. 5. With increasing the frequency f, the resonance peak shifts toward a higher field. Some excitation splitting at high frequency are likely due to the crystal misalignment relative to the magnetic field, however, the uncertainty associated with different peaks does not affect our estimates of the coupling constants including anisotropy parameters (see below). A small nonlinear feature in the $f(H)$ curve due to anisotropy can be seen most prominently for $\mathbf{H} \parallel c$. We obtain the zero-field frequency $f_0 = 28(4)$ GHz $= 0.12(2)$ meV and the g-factor $g_c = 2.11(2)$ by using the linear spin wave (LSW) theory to fit the ESR data (see Sec. III). For $\mathbf{H} \parallel a$ and $\mathbf{H} \parallel b$, g_a and g_b are 2.03(2) and 2.02(5), respectively.

III. SPIN WAVE THEORY

We discuss our LSW calculation applied to different phases in $Ba_3MnSb_2O_9$. Since the lattice distortion is small and there is no evidence in our INS experiments indicating that the magnetic order is incommensurate, the spin Hamiltonian in the quasi-2D *equilateral* triangular lattice is considered. As the difference in terms of the crystalline field between the two Mn^{2+} ($3d^5$) ions in the unit cell [aligning along the c axis as shown in Fig. 1(a)] is expected to be negligible, we consider the model with one site per unit cell, where the primitive lattice vectors are $\mathbf{a}_1 = \hat{\mathbf{x}}$, $\mathbf{a}_2 = -\frac{1}{2}\hat{\mathbf{x}} + \frac{\sqrt{3}}{2}\hat{\mathbf{y}}$, and $\mathbf{a}_3 = \frac{\mathbf{c}}{2}$. In practice, this merely means to consider $-1 \leqslant q_3 \leqslant 1$ in unit of $2\pi/c$ as the range of the first Brillouin zone for the third component of a wave vector $\mathbf{q}$. The spin-5/2 Hamiltonian in Eq. (1) has the antiferromagnetic intralayer

nearest-neighbor exchange interaction $J_1 > 0$, the intralayer next-nearest-neighbor exchange interaction J_2, the interlayer exchange interaction J_c, and the uniaxial single-ion anisotropy term D_z,

$$\mathcal{H} = J_1 \sum_{\langle \mathbf{r}, \mathbf{r}' \rangle_{NN}} \mathbf{S}_\mathbf{r} \cdot \mathbf{S}_{\mathbf{r}'} + J_2 \sum_{\langle \mathbf{r}, \mathbf{r}'' \rangle_{NNN}} \mathbf{S}_\mathbf{r} \cdot \mathbf{S}_{\mathbf{r}''}$$
$$+ J_c \sum_\mathbf{r} \mathbf{S}_\mathbf{r} \cdot \mathbf{S}_{\mathbf{r}+\frac{\mathbf{c}}{2}} + D_z \sum_\mathbf{r} \left(S_\mathbf{r}^z\right)^2. \quad (1)$$

Here, J_2 is included for better fitting, but the estimated strength turns out to be relatively small as shown below. The Fourier transformation of the exchange interaction, $J(\mathbf{q})$, is minimized at $\mathbf{q} = \mathbf{Q}$ with $\mathbf{Q} = \left(\frac{2\pi}{3}, \frac{2\pi}{3}, 2\pi\right)$ when $\frac{J_2}{J_1} \leqslant \frac{1}{8}$ and $\mathbf{Q} = (\pi, \pi, 2\pi)$ for $\frac{1}{8} < \frac{J_2}{J_1} < 1$ (see Appendix). The experimentally observed 120° magnetic structure is consistent with the former case.

To derive the LSW Hamiltonian H_{LSW}, the standard approach is used by first considering the local spin rotation $\mathbf{S} \to \tilde{\mathbf{S}}$ to set the local z axis to the orientation of the local ordered moment in the classical ground state, which is followed by the truncated Holstein-Primakoff transformation,

$$\tilde{S}_\mathbf{r}^z = S - b_\mathbf{r}^\dagger b_\mathbf{r}, \quad \tilde{S}_\mathbf{r}^+ \approx \sqrt{2S} b_\mathbf{r}, \quad \tilde{S}_\mathbf{r}^- \approx \sqrt{2S} b_\mathbf{r}^\dagger. \quad (2)$$

For a single-$\mathbf{Q}$ state, the site-dependent SO(3) transformation can be chosen as

$$\begin{pmatrix} S_\mathbf{r}^x \\ S_\mathbf{r}^y \\ S_\mathbf{r}^z \end{pmatrix} = \begin{pmatrix} -\sin \mathbf{Q} \cdot \mathbf{r} & 0 & \cos \mathbf{Q} \cdot \mathbf{r} \\ \cos \mathbf{Q} \cdot \mathbf{r} & 0 & \sin \mathbf{Q} \cdot \mathbf{r} \\ 0 & 1 & 0 \end{pmatrix} \begin{pmatrix} \tilde{S}_\mathbf{r}^x \\ \tilde{S}_\mathbf{r}^y \\ \tilde{S}_\mathbf{r}^z \end{pmatrix}. \quad (3)$$
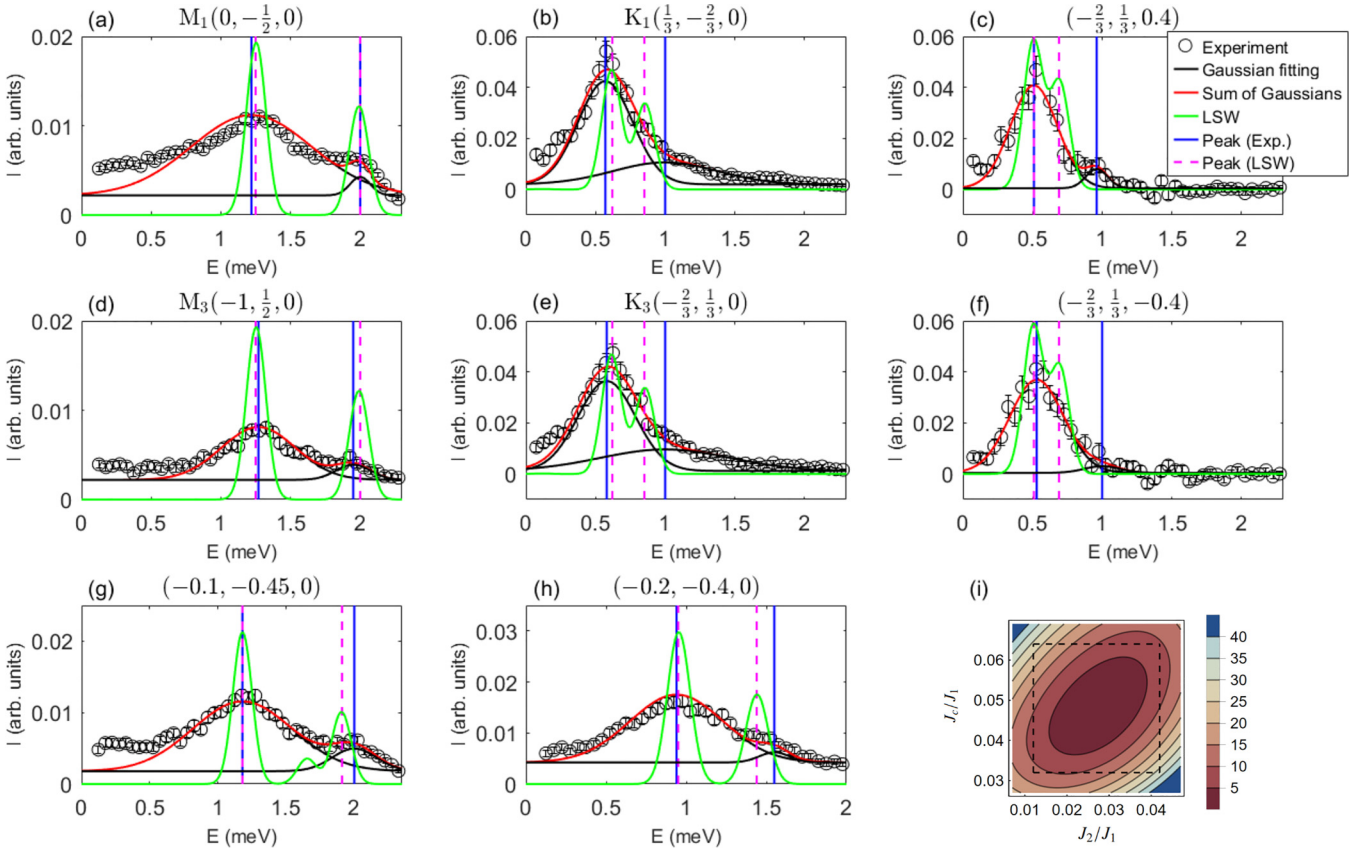
FIG. 4. [(a)–(h)] INS intensity-energy data for selected momenta used in our χ^2 analysis. The black and red lines show Gaussian fitting curves for individual peaks and the sum, respectively. The green line represents the LSW spectra convoluted with the instrumental energy resolution (0.07 meV). The vertical solid (dashed) lines indicate the peak positions estimated by the Gaussian fitting (LSW theory). (i) Contour plot of χ^2 on the J_c/J_1 and J_2/J_1 plane for $J_1 = 0.26$ meV. The rectangular indicates the confidence interval mentioned in the text, which is the region completely encompassing 95% of the cumulative χ^2 distribution.

By using the Fourier transformation $b_{\mathbf{r}} = N^{-1/2} \sum_{\mathbf{k}} e^{i\mathbf{k}\cdot\mathbf{r}} b_{\mathbf{k}}$, where the summation runs over the first Brillouin zone,

$$H_{\text{LSW}} = \sum_{\mathbf{k}} \frac{1}{2} \begin{pmatrix} b_{\mathbf{k}}^{\dagger} & b_{-\mathbf{k}} \end{pmatrix} \begin{pmatrix} A_{\mathbf{k}} & B_{\mathbf{k}} \\ B_{\mathbf{k}} & A_{\mathbf{k}} \end{pmatrix} \begin{pmatrix} b_{\mathbf{k}} \\ b_{-\mathbf{k}}^{\dagger} \end{pmatrix}, \quad (4)$$

where the coefficients $A_{\mathbf{k}}$ and $B_{\mathbf{k}}$ are given in Appendix. By performing the Bogoliubov transformation [54], $b_{\mathbf{k}} = u_{\mathbf{k}} \alpha_{\mathbf{k}} + v_{\mathbf{k}} \alpha_{-\mathbf{k}}^{\dagger}$ with $u_{\mathbf{k}}^2 - v_{\mathbf{k}}^2 = 1$, $u_{\mathbf{k}} = u_{\mathbf{k}}^* = u_{-\mathbf{k}}$, and $v_{\mathbf{k}} = v_{\mathbf{k}}^* = v_{-\mathbf{k}}$, the LSW Hamiltonian can be diagonalized as

$$H_{\text{LSW}} = \sum_{\mathbf{k}} \varepsilon_{\mathbf{k}} \left(\alpha_{\mathbf{k}}^{\dagger} \alpha_{\mathbf{k}} + \frac{1}{2} \right), \quad \varepsilon_{\mathbf{k}} = \sqrt{A_{\mathbf{k}}^2 - B_{\mathbf{k}}^2}. \quad (5)$$

We calculate the dynamical structure factor, $\mathcal{S}^{\mu\mu}(\mathbf{k}, \omega)$ with $\mu = x, y, z$, at $T = 0$ (see Appendix) and perform the χ^2 analysis to fit the theory with the INS data. In relation with $\varepsilon_{\mathbf{k}}$ in Eq. (5), $\mathcal{S}^{xx}(\mathbf{k}, \omega)$ and $\mathcal{S}^{yy}(\mathbf{k}, \omega)$ have peaks at the energy $\omega = \varepsilon_{\mathbf{k}\pm\mathbf{Q}}$ with the amplitudes proportional to $A_{\mathbf{k}\pm\mathbf{Q}} + B_{\mathbf{k}\pm\mathbf{Q}}$ while $\mathcal{S}^{xx}(\mathbf{k}, \omega)$ has a peak at $\omega = \varepsilon_{\mathbf{k}}$ with the amplitude proportional to $A_{\mathbf{k}} - B_{\mathbf{k}}$ [55]. In the χ^2 analysis, we include the following peaks as references, namely, the dominant peak (ϵ_1) and the secondary one (ϵ_2) at the M point, the dominant peak at the K point (ϵ_3), and dominant peaks at other low symmetry points, ϵ_4 at $\mathbf{q} = (-\frac{2}{3}, \frac{1}{3}, \pm 0.4)$, ϵ_5 at $\mathbf{q} = (-0.1, -0.45, 0)$, and ϵ_6 at $\mathbf{q} = (-0.2, -0.4, 0)$ (Fig. 4).

In addition, the information on the saturation field H_{sat} for a powder sample is included into the χ^2 analysis to constrain the fitting more strictly in terms of the overall energy scale. In theory, $g_c \mu_B H_{\text{sat}} = (9J + 4J_c + 2D_z)S$ for $\mathbf{H} \parallel c$. Experimentally, $H_{\text{sat}} \approx 49$ T is reported [50], for which we include the uncertainty of 1 T as the magnetization measurements in Ref. [50] did not reach the region where $M(H)$ is entirely flat. Here, except for the scattering data at M, the secondary INS peaks are not included in our χ^2 analysis due to relatively larger errors in the Gaussian fitting. Nevertheless, the result discussed below is mostly consistent also for these secondary INS peaks (Fig. 4).

In the analysis, we perform an iteration loop for the parameter estimation until convergence is achieved. Initially, we set $D_z = 0$ and estimate J_1, J_2, J_c, and g_c. In fact, the INS result in the available momentum region has almost no sign of $D_z \neq 0$. Although a gapped mode due to the anisotropy is expected at $\mathbf{q} = (1/3, 1/3, 1)$, this is outside of the momentum coverage in our INS measurements. Alternatively, we may use $\varepsilon_{\Gamma \pm \mathbf{Q}} \propto \sqrt{D_z/J_1}$ at Γ point, but the INS signal at this momentum is too weak to extract any information reliably from the INS measurements. Moreover, the gap turns out to be too small for our INS measurements.

To obtain the complementary information on D_z, the ESR measurements were refered. As a very sensitive probe for
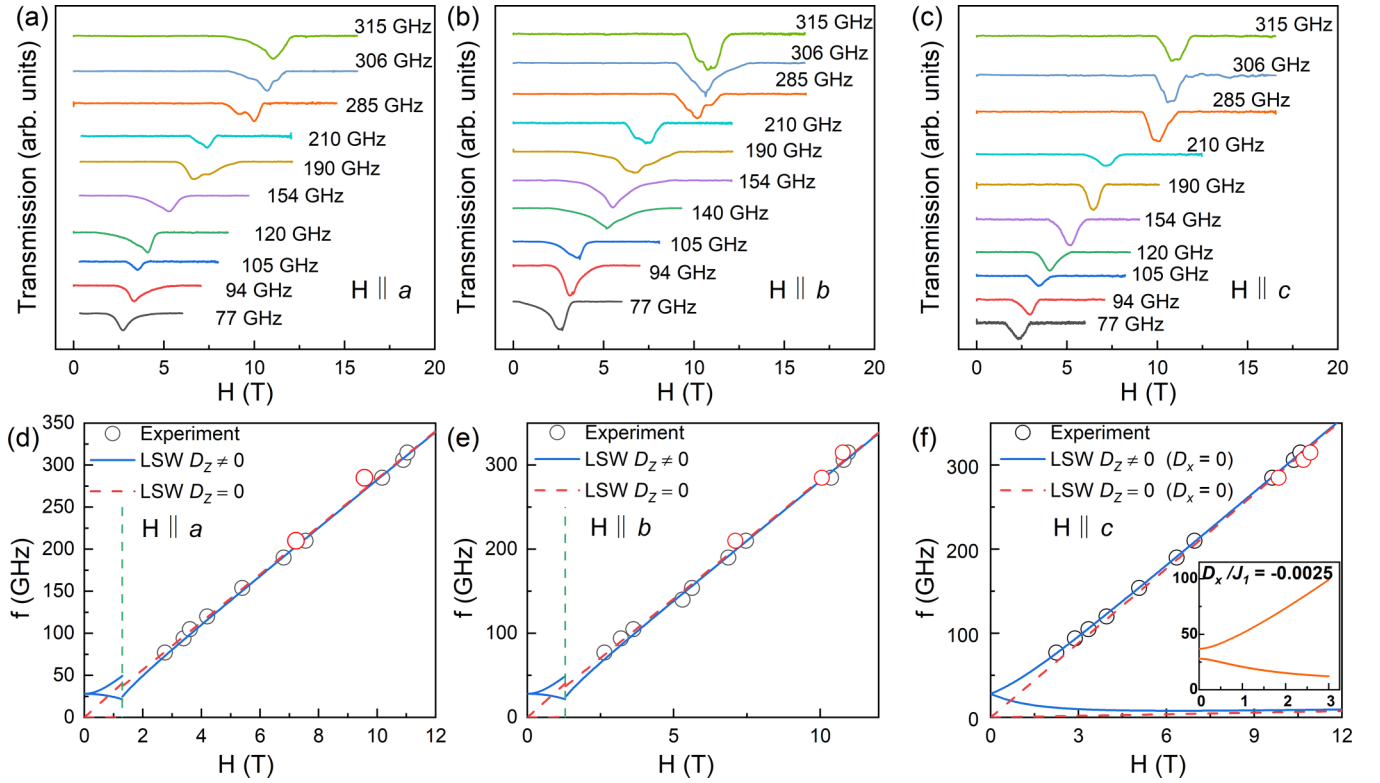
FIG. 5. [(a)–(c)] ESR spectra of $Ba_3MnSb_2O_9$ measured at 2 K for (a) **H** ∥ *a*, (b) **H** ∥ *b*, and (c) **H** ∥ *c*. [(d)–(f)] Resonance frequency *f* as a function of the magnetic field *H* for (d) **H** ∥ *a*, (e) **H** ∥ *b*, and (f) **H** ∥ *c*, the red circles are other peaks that split out at high frequencies. And the error bars are much smaller than the datapoint size. The solid (dashed) lines show the LSW theory for $D_z \neq 0$ ($D_z = 0$), respectively, where the vertical dashed lines in (d) and (e) indicate the spin flop transition predicted by the theory (as also suggested by dM/dH shown in Fig. 2). The inset in (f) shows the LSW theory of $f(H)$ for **H** ∥ *c* when small biaxial anisotropy is considered ($D_x/J_1 = -0.0025$).

magnetic anisotropy [56,57], the ESR absorption intensity is proportional to the imaginary part of the dynamical magnetic susceptibility, $\chi''_{\alpha\alpha}(\mathbf{k} = \Gamma, \omega) = \frac{1}{2}(1 - e^{-\beta\omega})S^{\alpha\alpha}(\mathbf{k} = \Gamma, \omega)$ [56–58]. For **H** ∥ *c*, the field-induced phase is the canted 120° state with the uniformly canting angle $\theta = \cos^{-1}\frac{h_c}{(4J_c + 9J_1 + 2D_z)S}$ with $h_c = g_c\mu_B H_c$ [Fig. 6(a)]. The resonance frequency $\omega_\pm(h_c)$ is independent of J_2 and given by (see Appendix) [59]

$$\omega_\pm(h_c) = \sqrt{\left(4J_c + \frac{9}{2}J_1\right)\left[2D_z S^2 + \frac{4J_c + \frac{9}{2}J_1 - 2D_z}{(4J_c + 9J_1 + 2D_z)^2}h_c^2\right]}$$
$$\mp \frac{9J_1}{2(4J_c + 9J_1 + 2D_z)}h_c. \quad (6)$$

Thus the χ^2 analysis of the INS data is followed by an evaluation of g_c and D_z/J_1 based on the ESR measurements using Eq. (6). We then return to the χ^2 analysis of the neutron scattering again, and the iterative process is repeated until the estimate of g_c converges. We thus obtain $J_1 = 0.26(1)$ meV, $J_c/J_1 = 0.048(16)$, $J_2/J_1 = 0.027(15)$ with the 95% confidence intervals ($\chi^2 \approx 0.6$ with four degrees of freedom). For reference, a contour plot of χ^2 on the plane of J_2/J_1 and J_c/J_1 for $J_1 = 0.26(1)$ meV is shown in Fig. 4(i). We also obtain $g_c = 2.11(2)$ and $D_z/J_1 = 0.0034(9)$ and the comparison against the ESR experiment for **H** ∥ *c* is shown in Fig. 5(c). Compared with $f(H)$ for $D_z = 0$, the LSW

theory for $D_z \neq 0$ can reproduce the subtle nonlinear field-dependence of $f(H)$, which allows for the precise determination of the small easy-plane anisotropy.

In Figs. 4(d)–4(f), the corresponding INS profiles are computed by the LSW theory based on the estimated coupling constants, which demonstrates a good agreement with the experiments shown in Figs. 4(a)–4(c). We also compute the ESR spectra for **H** ⊥ *c*, for which the model undergoes a spin-flop transition from the in-plane coplanar (distorted 120°) state in the *ab* plane to a distorted umbrellalike noncoplanar phase [Figs. 6(c) and 6(d)]. The transition takes place at around $H_\perp^{sf} \approx 4S\sqrt{J_1 D_z}/(g_\perp\mu_B) = 1.3(2)$ T [59]. Indeed, the signal of this spin-flop transition can be seen as a small peak in dM/dH, Fig. 2(d), as mentioned before. Our ESR data for **H** ⊥ *c* belongs to the high-field noncoplanar phase above the spin-flop transition, which displays an even milder nonlinearity than the case for **H** ∥ *c*. As shown in Figs. 5(a) and 5(b), our LSW theory for **H** ⊥ *c* (see Appendix) can reproduce the magnetic field dependence of the resonance frequency also in this case.

Finally, from the crystalline field symmetry of a monoclinic system, the biaxial anisotropy may be expected [50]. The space group is $C2/c$ and Mn^{2+} is at the symmetry center of MnO_6, which can lead to $D_x(S_\mathbf{r}^x)^2$ in addition to $D_z(S_\mathbf{r}^z)^2$ due to the distortion of regular octahedron MnO_6. By examining the effect of the biaxial anisotropy due to small $D_x \neq 0$ with the LSW, we find that this causes a splitting of the degenerate
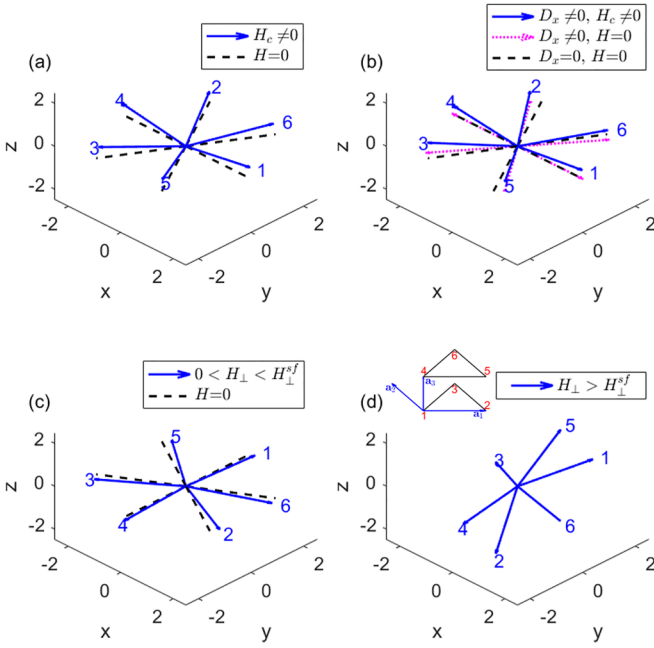
FIG. 6. Schematic spin configurations of the classical ground states. The sublattice indices 1–6 are shown in the inset of (d). (a) Uniformly canted (umbrella) 120° state towards the direction of $\mathbf{H} \parallel c$ for $D_x = 0$ ($D_z \neq 0$) in comparison with the in-plane 120° state in zero field. (b) Distorted in-plane and umbrella 120° states due to biaxial anisotropy ($D_x, D_z \neq 0$) with and without a magnetic field $\mathbf{H} \parallel c$. To illustrate the deformation clearly, the assumed anisotropy is considerably larger than the reality. (c) Distorted 120° state due to the in-plane magnetic field $\mathbf{H} \perp c$. (d) High-field noncoplanar state for $\mathbf{H} \perp c$.

zero-field ESR resonance frequency [see the inset of Fig. 5(f)]. However, the zero-field frequency $f_0 = 28(4)$ GHz is so small that the possible small splitting is inaccessible in our ESR measurements.

IV. CONCLUSIONS

In summary, we have presented a comprehensive experimental and theoretical study on Ba$_3$MnSb$_2$O$_9$, an easy-plane $S = 5/2$ quasi-2D TLAHM with a small monoclinic crystal distortion. We have obtained a reliable set of estimates for the coupling constants of the spin Hamiltonian by analyzing our INS and ESR data using the LSW theory, thereby established very close proximity of Ba$_3$MnSb$_2$O$_9$ to the ideal isotropic TLAHM. The easy-plane anisotropy is so small that it can only be detected by ESR in our study.

The observed linewidth in the INS experiment is much broader than the instrument resolution. Although it is rather difficult at the current stage to make a conclusive statement about the origin of the broadening, given that the LSW calculation is performed at $T = 0$, the broadening might be due to thermal fluctuation where frustration-induced low-energy states may give rise to a strong contribution. The broadening may also be caused by a multiple domain effect, especially if the true magnetic order turns out to be incommensurate, although the monoclinic lattice distortion is so small that the possible deviation, if any, of the ordering

wave vector from the K point is beyond our experimental resolution. Another possible source of the broadening is the Sb deficiency $\approx 4\%$ in our sample. Although such deficiency may be safely regarded as very small, it might induce small exchange randomness through local deformation, causing the broadening. In the meantime, we could safely exclude quantum-mechanical magnon decay effects as the source of the broadening because the magnetic moment $4.9\,\mu_B$ obtained by single-crystal diffraction fitting is quite close to the classical value $g_{ab}S\mu_B \simeq 5.05\,\mu_B$. In fact, as discussed by Mourigal *et al.*, the line-broadening and the spectral renormalization in the 2D TLAHM are known to be much smaller than the quantum limit $S = 1/2$ already for $S = 3/2$ [53].

It is interesting to note that the peak near T_N of the specific heat of our high-quality single-crystal samples [Fig. 2(a)] is much rounder than that of the polycrystalline data reported in the literature [49], which is opposite to what one would normally expect. Furthermore, $T_N \approx 7$ K for our samples is significantly lower than one for the polycrystalline data, 10.2 K [49].

While the Sb deficiency due to the low melting point may be the possible origin, it is also possible that the high quality of our samples makes the intrinsic frustration effect come into play, yielding a higher degree of nearly degenerate low-energy manifold than in polycrystalline samples.

Because of the extremely small anisotropy, Ba$_3$MnSb$_2$O$_9$ may have the potential to study Z- or Z_2-vortex excitations experimentally. According to the structure of the 120° ordering ground state, a homotopy analysis shows that the 2D TLAHM bears topologically-stable Z-vortices for the TLAHM with uniaxial anisotropy and Z_2 vortices for the isotropic Heisenberg model [7]. The close proximity of Ba$_3$MnSb$_2$O$_9$ to the isotropic model may allow for studying phenomena associated with these vortices experimentally, such as the conjectured Kosterlitz-Thouless-like transition due to vortex-pair (un)binding [7] and crossover phenomena between Z or Z_2 vortices [42]. As a potential signature of Z_2 vortices, it has been discussed in the literature that the Kosterlitz-Thouless-like transition may induce a divergent spin-current conductivity [40]. In addition, the dynamical spin structure factor may yield a characteristic central peak [43,45,46], as discussed experimentally in the quasi-2D TLAHM material with easy-axis anisotropy NaCrO$_2$ [41,60]. Because of the difference in the anisotropy type, Ba$_3$MnSb$_2$O$_9$ will provide a distinct experimental platform to explore topological defects in a triangular lattice system. Compared with another material well-studied regarding Z_2-vortices is the $S = 1$ triangular lattice material NiGa$_2$S$_4$, the easy plane anisotropy relative to the largest exchange coupling, $D_z/J_1 = 0.0034(9)$, is even smaller in Ba$_3$MnSb$_2$O$_9$ ($D_z/J_3 \approx 0.035$ in NiGa$_2$S$_4$) [45,61,62]. In addition, with $S = 1$, quantum fluctuation in NiGa$_2$S$_4$ is believed to play an important role, whereas in Ba$_3$MnSb$_2$O$_9$ with $S = 5/2$, one could focus on thermal physics of topological defects.

We hope that our work establishing Ba$_3$MnSb$_2$O$_9$ as a promising candidate model material in this context will trigger similar efforts towards more challenging experiments in search for signatures of unconventional topological excitations.

APPENDIX: DETAILS OF THE LSW THEORY

1. Zero magnetic field ($D_x = 0$)

At zero magnetic field, the classical ground state for $D_x = 0$ can be obtained by minimizing the Fourier transform of the exchange interaction, $J(\mathbf{q}) = 2J_1(\cos q_1 + \cos q_2 + \cos(q_1 + q_2)) + 2J_2(\cos(2q_1 + q_2) + \cos(q_2 - q_1) + \cos(q_1 + 2q_2)) + 2J_c \cos(q_3/2)$. The wave vector $\mathbf{q} = q_1\mathbf{b}_1 + q_2\mathbf{b}_2 + \frac{q_3}{2}\mathbf{b}_3$ is expressed as (q_1, q_2, q_3), where $\mathbf{b}_i$ are reciprocal unit vectors. For a single $\mathbf{Q}$ state, the coefficients $A_\mathbf{k}$ and $B_\mathbf{k}$ in Eq. (4) are

$$\frac{A_\mathbf{k}}{S} = J_1[(1 + \cos Q_1)\cos k_1 + (1 + \cos Q_2)\cos k_2 + (1 + \cos(Q_1 + Q_2))\cos(k_1 + k_2)]$$

$$- 2J_1(\cos Q_1 + \cos Q_2 + \cos(Q_1 + Q_2)) + 2J_c + 2J_2[\cos(2k_1 + k_2) + \cos(k_2 - k_1) + \cos(k_1 + 2k_2) - 3] + D_z,$$

$$\frac{B_\mathbf{k}}{S} = -J_1[(1 - \cos Q_1)\cos k_1 + (1 - \cos Q_2)\cos k_2 + (1 - \cos(Q_1 + Q_2))\cos(k_1 + k_2)] - 2J_c \cos(k_3/2) - D_z. \quad \text{(A1)}$$

The dynamical spin structure factor $T = 0$ is

$$\mathcal{S}^{\alpha\beta}(\mathbf{k}, \omega) = \int_{-\infty}^{\infty} \frac{dt}{2\pi} e^{i\omega t} \frac{1}{N} \sum_{ij} e^{-i\mathbf{k} \cdot (\mathbf{r}_i - \mathbf{r}_j)} \langle 0|S_i^\alpha(t) S_j^\beta(0)|0\rangle, \quad \text{(A2)}$$

where $|0\rangle$ is the vacuum of the Bogoliubov boson. We find

$$\mathcal{S}^{xx}(\mathbf{k}, \omega) = \mathcal{S}^{yy}(\mathbf{k}, \omega) = \frac{S}{8} \sum_\mathbf{q} \frac{A_\mathbf{q} + B_\mathbf{q}}{\varepsilon_\mathbf{q}} \delta(\omega - \varepsilon_\mathbf{q})(\delta_{\mathbf{q}, \mathbf{k}+\mathbf{Q}} + \delta_{\mathbf{q}, \mathbf{k}-\mathbf{Q}})$$

$$+ \left[\frac{1}{4}NS^2 - \frac{1}{2}S \sum_\mathbf{q} \frac{B_\mathbf{q}^2}{(A_\mathbf{q} + \varepsilon_\mathbf{q})^2 - B_\mathbf{q}^2} \right] \delta(\omega)(\delta_{\mathbf{k}, \mathbf{Q}} + \delta_{\mathbf{k}, -\mathbf{Q}}),$$

$$\mathcal{S}^{zz}(\mathbf{k}, \omega) = \frac{S}{2} \frac{A_\mathbf{k} - B_\mathbf{k}}{\varepsilon_\mathbf{k}} \delta(\omega - \varepsilon_\mathbf{k}). \quad \text{(A3)}$$

2. H ∥ c ($D_x = 0$)

For nonzero magnetic field parallel to the c axis and $D_x = 0$, the classical ground state is the 120° state with the uniformly canting angle $\theta = \cos^{-1} \frac{h_c}{(4J_c + 9J_1 + 2D_z)S}$ [Fig. 6(a)]. The corresponding LSW Hamiltonian is

$$H_{\text{LSW}}^{\mathbf{H}\|c} = \sum_\mathbf{k} \frac{1}{2} (b_\mathbf{k}^\dagger \ b_{-\mathbf{k}}) \begin{pmatrix} A_\mathbf{k}^{\mathbf{H}\|c} + C_\mathbf{k}^{\mathbf{H}\|c} & B_\mathbf{k}^{\mathbf{H}\|c} \\ B_\mathbf{k}^{\mathbf{H}\|c} & A_\mathbf{k}^{\mathbf{H}\|c} - C_\mathbf{k}^{\mathbf{H}\|c} \end{pmatrix} \begin{pmatrix} b_\mathbf{k} \\ b_{-\mathbf{k}}^\dagger \end{pmatrix}, \quad \text{(A4)}$$

with

$$A_\mathbf{k}^{\mathbf{H}\|c} = J_1 S\left[3 - 9\cos^2\theta + \left(\tfrac{1}{2} - \tfrac{3}{2}\cos^2\theta\right)(\cos k_1 + \cos k_2 + \cos(k_1 + k_2))\right]$$

$$+ 2J_2 S[\cos(2k_1 + k_2) + \cos(k_2 - k_1) + \cos(k_1 + 2k_2) - 3]$$

$$+ J_c S(-2\cos^2\theta \cos(k_3/2) - 4\cos^2\theta + 2) + D_z S(1 - 3\cos^2\theta) + h_c \cos\theta, \quad \text{(A5)}$$

$$B_\mathbf{k}^{\mathbf{H}\|c} = J_1 S(\cos k_1 + \cos k_2 + \cos(k_1 + k_2))\left(-\tfrac{3}{2} + \tfrac{3}{2}\cos^2\theta\right) - D_z S \sin^2\theta + J_c S \cos(k_3/2)(2\cos^2\theta - 2), \quad \text{(A6)}$$

$$C_\mathbf{k}^{\mathbf{H}\|c} = -\cos\theta\sqrt{3}J_1 S[\sin k_1 + \sin k_2 - \sin(k_1 + k_2)]. \quad \text{(A7)}$$

The spin wave dispersion is $\varepsilon_\mathbf{k}^{\mathbf{H}\|c} = \sqrt{(A_\mathbf{k}^{\mathbf{H}\|c})^2 - (B_\mathbf{k}^{\mathbf{H}\|c})^2} + C_\mathbf{k}^{\mathbf{H}\|c}$, from which the resonance energy in Eq. (6) can be obtained.

3. $H \perp c$ ($D_x = 0$)

The classical ground states discussed in the following cases are not a single-$\mathbf{Q}$ state. Thus we derive a general spin-wave Hamiltonian for any six-sublattice order by performing the sublattice ($1 \leqslant \eta \leqslant 6$)-dependent SO(3) transformation $R(\eta)$, where the positions of sublattices are shown in the inset in Fig. 6(d). For every site i in the ηth sublattice, we consider

$$\begin{pmatrix} S_i^x \\ S_i^y \\ S_i^z \end{pmatrix} = R(\eta) \begin{pmatrix} \widetilde{S}_i^x \\ \widetilde{S}_i^y \\ \widetilde{S}_i^z \end{pmatrix}. \tag{A8}$$

The resulting LSW Hamiltonian is

$$H_{\mathrm{LSW}}^{\mathrm{gen}} = \sum_{\mathbf{k}} \left(\Psi_{\mathbf{k}}^{\mathrm{gen}} \right)^{\dagger} H_{\mathbf{k}}^{\mathrm{gen}} \Psi_{\mathbf{k}}^{\mathrm{gen}} = \sum_{\mathbf{k}} \frac{1}{2} \left(\Psi_{\mathbf{k}}^{\mathrm{gen}} \right)^{\dagger} \begin{pmatrix} A_{\mathbf{k}}^{\mathrm{gen}} + C_{\mathbf{k}}^{\mathrm{gen}} & B_{\mathbf{k}}^{\mathrm{gen}} \\ \left(B_{\mathbf{k}}^{\mathrm{gen}} \right)^{\dagger} & A_{\mathbf{k}}^{\mathrm{gen}} - C_{\mathbf{k}}^{\mathrm{gen}} \end{pmatrix} \Psi_{\mathbf{k}}^{\mathrm{gen}}, \tag{A9}$$

where $\Psi_{\mathbf{k}}^{\mathrm{gen}} = (b_{1,\mathbf{k}}, \dots, b_{6,\mathbf{k}}, b_{1,-\mathbf{k}}^{\dagger}, \dots, b_{6,-\mathbf{k}}^{\dagger})^{\mathrm{T}}$ and

$$A_{\mathbf{k}}^{\mathrm{gen}} = \begin{pmatrix} \gamma^{(2)}{}_{\mathbf{k}}(1) + \gamma^{(1)}{}_{\mathbf{k}}(3) & \gamma^{(4)}{}_{\mathbf{k}}(1) & \gamma^{(4)*}{}_{\mathbf{k}}(3) & \gamma^{(9)}{}_{\mathbf{k}}(1) & 0 & 0 \\ \gamma^{(4)*}{}_{\mathbf{k}}(1) & \gamma^{(2)}{}_{\mathbf{k}}(2) + \gamma^{(1)}{}_{\mathbf{k}}(1) & \gamma^{(4)}{}_{\mathbf{k}}(2) & 0 & \gamma^{(9)}{}_{\mathbf{k}}(2) & 0 \\ \gamma^{(4)}{}_{\mathbf{k}}(3) & \gamma^{(4)*}{}_{\mathbf{k}}(2) & \gamma^{(2)}{}_{\mathbf{k}}(3) + \gamma^{(1)}{}_{\mathbf{k}}(2) & 0 & 0 & \gamma^{(9)}{}_{\mathbf{k}}(3) \\ \gamma^{(9)}{}_{\mathbf{k}}(1) & 0 & 0 & \gamma^{(2)}{}_{\mathbf{k}}(4) + \gamma^{(1)}{}_{\mathbf{k}}(6) & \gamma^{(4)}{}_{\mathbf{k}}(4) & \gamma^{(4)*}{}_{\mathbf{k}}(6) \\ 0 & \gamma^{(9)}{}_{\mathbf{k}}(2) & 0 & \gamma^{(4)*}{}_{\mathbf{k}}(4) & \gamma^{(2)}{}_{\mathbf{k}}(5) + \gamma^{(1)}{}_{\mathbf{k}}(4) & \gamma^{(4)}{}_{\mathbf{k}}(5) \\ 0 & 0 & \gamma^{(9)}{}_{\mathbf{k}}(3) & \gamma^{(4)}{}_{\mathbf{k}}(6) & \gamma^{(4)*}{}_{\mathbf{k}}(5) & \gamma^{(2)}{}_{\mathbf{k}}(6) + \gamma^{(1)}{}_{\mathbf{k}}(5) \end{pmatrix}, \tag{A10}$$

$$B_{\mathbf{k}}^{\mathrm{gen}} = \begin{pmatrix} \gamma^{(3)}{}_{\mathbf{k}}(1) & \gamma^{(5)}{}_{\mathbf{k}}(1) + \gamma^{(6)}{}_{\mathbf{k}}(1) & \gamma^{(5)*}{}_{\mathbf{k}}(3) - \gamma^{(6)*}{}_{\mathbf{k}}(3) & \gamma^{(8)}{}_{\mathbf{k}}(1) & 0 & 0 \\ \gamma^{(5)*}{}_{\mathbf{k}}(1) - \gamma^{(6)*}{}_{\mathbf{k}}(1) & \gamma^{(3)}{}_{\mathbf{k}}(2) & \gamma^{(5)}{}_{\mathbf{k}}(2) + \gamma^{(6)}{}_{\mathbf{k}}(2) & 0 & \gamma^{(8)}{}_{\mathbf{k}}(2) & 0 \\ \gamma^{(5)}{}_{\mathbf{k}}(3) + \gamma^{(6)}{}_{\mathbf{k}}(3) & \gamma^{(5)*}{}_{\mathbf{k}}(2) - \gamma^{(6)*}{}_{\mathbf{k}}(2) & \gamma^{(3)}{}_{\mathbf{k}}(3) & 0 & 0 & \gamma^{(8)}{}_{\mathbf{k}}(3) \\ \gamma^{(8)}{}_{\mathbf{k}}(1) & 0 & 0 & \gamma^{(3)}{}_{\mathbf{k}}(4) & \gamma^{(5)}{}_{\mathbf{k}}(4) + \gamma^{(6)}{}_{\mathbf{k}}(4) & \gamma^{(5)*}{}_{\mathbf{k}}(6) - \gamma^{(6)*}{}_{\mathbf{k}}(6) \\ 0 & \gamma^{(8)}{}_{\mathbf{k}}(2) & 0 & \gamma^{(5)*}{}_{\mathbf{k}}(4) - \gamma^{(6)*}{}_{\mathbf{k}}(4) & \gamma^{(3)}{}_{\mathbf{k}}(5) & \gamma^{(5)}{}_{\mathbf{k}}(5) + \gamma^{(6)}{}_{\mathbf{k}}(5) \\ 0 & 0 & \gamma^{(8)}{}_{\mathbf{k}}(3) & \gamma^{(5)}{}_{\mathbf{k}}(6) + \gamma^{(6)}{}_{\mathbf{k}}(6) & \gamma^{(5)*}{}_{\mathbf{k}}(5) - \gamma^{(6)*}{}_{\mathbf{k}}(5) & \gamma^{(3)}{}_{\mathbf{k}}(6) \end{pmatrix}, \tag{A11}$$

$$C_{\mathbf{k}}^{\mathrm{gen}} = \begin{pmatrix} 0 & \gamma^{(7)}{}_{\mathbf{k}}(1) & \gamma^{(7)*}{}_{\mathbf{k}}(3) & \gamma^{(10)}{}_{\mathbf{k}}(1) & 0 & 0 \\ \gamma^{(7)*}{}_{\mathbf{k}}(1) & 0 & \gamma^{(7)}{}_{\mathbf{k}}(2) & 0 & \gamma^{(10)}{}_{\mathbf{k}}(2) & 0 \\ \gamma^{(7)}{}_{\mathbf{k}}(3) & \gamma^{(7)*}{}_{\mathbf{k}}(2) & 0 & 0 & 0 & \gamma^{(10)}{}_{\mathbf{k}}(3) \\ -\gamma^{(10)}{}_{\mathbf{k}}(1) & 0 & 0 & 0 & \gamma^{(7)}{}_{\mathbf{k}}(4) & \gamma^{(7)*}{}_{\mathbf{k}}(6) \\ 0 & -\gamma^{(10)}{}_{\mathbf{k}}(2) & 0 & \gamma^{(7)*}{}_{\mathbf{k}}(4) & 0 & \gamma^{(7)}{}_{\mathbf{k}}(5) \\ 0 & 0 & -\gamma^{(10)}{}_{\mathbf{k}}(3) & \gamma^{(7)}{}_{\mathbf{k}}(6) & \gamma^{(7)*}{}_{\mathbf{k}}(5) & 0 \end{pmatrix}. \tag{A12}$$

Here, to define the matrix elements, we introduce the convention for the C_3 rotation of sublattice indices as η^+ ($\eta^+ = 2, 3, 1$ for $\eta = 1, 2, 3$ and $\eta^+ = 5, 6, 4$ for $\eta = 4, 5, 6$) as well as one for the Z_2 reflection exchanging the even and odd layers as $\bar{\eta}$ ($\bar{\eta} = 4, 5, 6$ for $\eta = 1, 2, 3$ and $\bar{\bar{\eta}} = \eta$). With these notations, we list the (components of) matrix elements appearing in Eqs. (A10)–(A12):

$$\gamma^{(1)}{}_{\mathbf{k}}(\eta) = -3J_1 S \sum_v R_{v3}(\eta) R_{v3}(\eta^+),$$

$$\gamma^{(2)}{}_{\mathbf{k}}(\eta) = \gamma^{(1)}{}_{\mathbf{k}}(\eta) - 2J_c S \sum_v R_{v3}(\eta) R_{v3}(\bar{\eta}) + D_z S \left(-2R_{33}^2(\eta) + R_{31}^2(\eta) + R_{32}^2(\eta) \right) + h_c R_{33}(\eta) + h_\perp R_{13}(\eta)$$

$$+ D_x S \left(-2R_{13}^2(\eta) + R_{11}^2(\eta) + R_{12}^2(\eta) \right) + 2J_2 S (\cos(2k_1 + k_2) + \cos(k_2 - k_1) + \cos(k_1 + 2k_2) - 3),$$

$$\gamma^{(3)}{}_{\mathbf{k}}(\eta) = D_z S \left(R_{31}^2(\eta) - R_{32}^2(\eta) + i2R_{31}(\eta) R_{32}(\eta) \right) + D_x S \left(R_{11}^2(\eta) - R_{12}^2(\eta) + i2R_{11}(\eta) R_{12}(\eta) \right),$$

$$\gamma^{(4)}{}_{\mathbf{k}}(\eta) = J_1 \frac{S}{2} f_{\mathbf{k}} \sum_v (R_{v1}(\eta) R_{v1}(\eta^+) + R_{v2}(\eta) R_{v2}(\eta^+)),$$

$$\gamma^{(5)}{}_{\mathbf{k}}(\eta) = J_1 \frac{S}{2} f_{\mathbf{k}} \sum_v (R_{v1}(\eta) R_{v1}(\eta^+) - R_{v2}(\eta) R_{v2}(\eta^+)),$$

$$\gamma^{(6)}{}_{\mathbf{k}}(\eta) = iJ_1 \frac{S}{2} f_{\mathbf{k}} \sum_v (R_{v1}(\eta)R_{v2}(\eta^+) + R_{v2}(\eta)R_{v1}(\eta^+)),$$

$$\gamma^{(7)}{}_{\mathbf{k}}(\eta) = -iJ_1 \frac{S}{2} f_{\mathbf{k}} \sum_v (R_{v1}(\eta)R_{v2}(\eta^+) - R_{v2}(\eta)R_{v1}(\eta^+)),$$

$$\gamma^{(8)}{}_{\mathbf{k}}(\eta) = J_c S \cos(k_3/2) \sum_v (R_{v1}(\eta)R_{v1}(\bar{\eta}) - R_{v2}(\eta)R_{v2}(\bar{\eta})) + iJ_c S \cos(k_3/2) \sum_v (R_{v1}(\eta)R_{v2}(\bar{\eta}) + R_{v2}(\eta)R_{v1}(\bar{\eta})),$$

$$\gamma^{(9)}{}_{\mathbf{k}}(\eta) = J_c S \cos(k_3/2) \sum_v (R_{v1}(\eta)R_{v1}(\bar{\eta}) + R_{v2}(\eta)R_{v2}(\bar{\eta})),$$

$$\gamma^{(10)}{}_{\mathbf{k}}(\eta) = -iJ_c S \cos(k_3/2) \sum_v (R_{v1}(\eta)R_{v2}(\bar{\eta}) - R_{v2}(\eta)R_{v1}(\bar{\eta})), \tag{A13}$$

with $f_{\mathbf{k}} = e^{ik_1} + e^{ik_2} + e^{-i(k_1+k_2)}$. $H_{\mathrm{LSW}}^{\mathrm{gen}}$ can be diagonalized by the general method for the Bogoliubov transformation for bosons [54,63]. By checking the asymptotic behavior of $\mathcal{S}^{\alpha\alpha}(\mathbf{k}, \omega)$ as goes to the Γ point, we evaluate the ESR resonance frequency as shown in Fig. 5.

4. Effect of biaxial anisotropy ($D_x \neq 0$)

We examine the effect of $D_x \neq 0$ for zero field and for nonzero field with $\mathbf{H} \parallel c$. We obtain the classical ground states by a numerically optimization of a six-sublattice ansatz of the classical mean-field energy. The main effect is distortion of the $120°$ structure towards the second principle axis (i.e., the x axis for $D_x < 0$) of the anisotropy [see Fig. 6(b)]. We find that the ground state allows for setting, in terms of the spherical coordinates of the ordered moments, $\theta_2 = \theta_3$, $\theta_{\bar{\eta}} = \theta_\eta$, $\phi_1 = 0$, $\phi_2 + \phi_3 = \pi$, and $\phi_{\bar{\eta}} = \phi_\eta + \pi$ without losing generality. The subsequent analysis can be carried out using the same LSW Hamiltonian as above, $H_{\mathrm{LSW}}^{\mathrm{gen}}$.

[1] P. W. Anderson, Resonating valence bonds: A new kind of insulator?, Mater. Res. Bull. **8**, 153 (1973).

[2] S.-H. Lee, C. Broholm, W. Ratcliff, G. Gasparovic, Q. Huang, T. H. Kim, and S.-W. Cheong, Emergent excitations in a geometrically frustrated magnet, Nature (London) **418**, 856 (2002).

[3] L. Balents, Spin liquids in frustrated magnets, Nature (London) **464**, 199 (2010).

[4] R. Moessner and A. P. Ramirez, Geometrical frustration, Phys. Today **59**, 24 (2006).

[5] J. Ma, Spins don't align here, Nat. Phys. **19**, 922 (2023).

[6] H. Jeschke, I. Opahle, H. Kandpal, R. Valentí, H. Das, T. Saha-Dasgupta, O. Janson, H. Rosner, A. Brühl, B. Wolf, M. Lang, J. Richter, S. Hu, X. Wang, R. Peters, T. Pruschke, and A. Honecker, Multistep approach to microscopic models for frustrated quantum magnets: The case of the natural mineral azurite, Phys. Rev. Lett. **106**, 217201 (2011).

[7] H. Kawamura and S. Miyashita, Phase transition of the two-dimensional Heisenberg antiferromagnet on the triangular lattice, J. Phys. Soc. Jpn. **53**, 4138 (1984).

[8] K. Yokota, N. Kurita, and H. Tanaka, Magnetic phase diagram of the $S{=}1/2$ triangular-lattice Heisenberg antiferromagnet Ba$_3$CoNb$_2$O$_9$, Phys. Rev. B **90**, 014403 (2014).

[9] Y.-D. Li, X. Wang, and G. Chen, Anisotropic spin model of strong spin-orbit coupled triangular antiferromagnets, Phys. Rev. B **94**, 035107 (2016).

[10] C. Kim, A. Y. Matsuura, Z.-X. Shen, N. Motoyama, H. Eisaki, S. Uchida, T. Tohyama, and S. Maekawa, Observation of spin-charge separation in one-dimensional SrCuO$_2$, Phys. Rev. Lett. **77**, 4054 (1996).

[11] A. V. Chubukov, T. Senthil, and S. Sachdev, Universal magnetic properties of frustrated quantum antiferromagnets in two dimensions, Phys. Rev. Lett. **72**, 2089 (1994).

[12] A. V. Chubukov and D. I. Golosov, Quantum theory of an antiferromagnet on a triangular lattice in a magnetic field, J. Phys.: Condens. Matter **3**, 69 (1991).

[13] A. L. Chernyshev and M. E. Zhitomirsky, Spin waves in a triangular lattice antiferromagnet: Decays, spectrum renormalization, and singularities, Phys. Rev. B **79**, 144416 (2009).

[14] M. Li, A. Zelenskiy, J. A. Quilliam, Z. L. Dun, H. D. Zhou, M. L. Plumer, and G. Quirion, Magnetoelastic coupling and the magnetization plateau in Ba$_3$CoSb$_2$O$_9$, Phys. Rev. B **99**, 094408 (2019).

[15] R. Coldea, D. A. Tennant, and Z. Tylczynski, Extended scattering continua characteristic of spin fractionalization in the two-dimensional frustrated quantum magnet Cs$_2$CuCl$_4$ observed by neutron scattering, Phys. Rev. B **68**, 134424 (2003).

[16] B. Fåk, S. Bieri, E. Canévet, L. Messio, C. Payen, M. Viaud, C. Guillot-Deudon, C. Darie, J. Ollivier, and P. Mendels, Evidence for a spinon Fermi surface in the triangular $S = 1$ quantum spin liquid Ba$_3$NiSb$_2$O$_9$, Phys. Rev. B **95**, 060402(R) (2017).

[17] J. Oh, M. D. Le, J. Jeong, J.-h. Lee, H. Woo, W.-Y. Song, T. G. Perring, W. J. L. Buyers, S.-W. Cheong, and J.-G. Park, Magnon breakdown in a two dimensional triangular lattice Heisenberg antiferromagnet of multiferroic LuMnO$_3$, Phys. Rev. Lett. **111**, 257202 (2013).

[18] T. Kim, J. C. Leiner, K. Park, J. Oh, H. Sim, K. Iida, K. Kamazawa, and J.-G. Park, Renormalization of spin

excitations in hexagonal $HoMnO_3$ by magnon-phonon coupling, Phys. Rev. B **97**, 201113(R) (2018).

[19] O. A. Starykh, A. V. Chubukov, and A. G. Abanov, Flat spin-wave dispersion in a triangular antiferromagnet, Phys. Rev. B **74**, 180403(R) (2006).

[20] A. L. Chernyshev and M. E. Zhitomirsky, Magnon decay in noncollinear quantum antiferromagnets, Phys. Rev. Lett. **97**, 207202 (2006).

[21] Y. Doi, Y. Hinatsu, and K. Ohoyama, Structural and magnetic properties of pseudo-two-dimensional triangular antiferromagnets $Ba_3MSb_2O_9$ (M = Mn, Co, and Ni), J. Phys.: Condens. Matter **16**, 8923 (2004).

[22] T. Susuki, N. Kurita, T. Tanaka, H. Nojiri, A. Matsuo, K. Kindo, and H. Tanaka, Magnetization process and collective excitations in the $S=1/2$ triangular-lattice Heisenberg antiferromagnet $Ba_3CoSb_2O_9$, Phys. Rev. Lett. **110**, 267201 (2013).

[23] Y. Shirata, H. Tanaka, A. Matsuo, and K. Kindo, Experimental realization of a spin-1/2 triangular-lattice Heisenberg antiferromagnet, Phys. Rev. Lett. **108**, 057205 (2012).

[24] G. Koutroulakis, T. Zhou, Y. Kamiya, J. D. Thompson, H. D. Zhou, C. D. Batista, and S. E. Brown, Quantum phase diagram of the $S = \frac{1}{2}$ triangular-lattice antiferromagnet $Ba_3CoSb_2O_9$, Phys. Rev. B **91**, 024410 (2015).

[25] G. Quirion, M. Lapointe-Major, M. Poirier, J. A. Quilliam, Z. L. Dun, and H. D. Zhou, Magnetic phase diagram of $Ba_3CoSb_2O_9$ as determined by ultrasound velocity measurements, Phys. Rev. B **92**, 014414 (2015).

[26] Y. Kamiya, L. Ge, T. Hong, Y. Qiu, D. L. Quintero-Castro, Z. Lu, H. B. Cao, M. Matsuda, E. S. Choi, C. D. Batista, M. Mourigal, H. D. Zhou, and J. Ma, The nature of spin excitations in the one-third magnetization plateau phase of $Ba_3CoSb_2O_9$, Nat. Commun. **9**, 2666 (2018).

[27] X. Z. Liu, O. Prokhnenko, D. Yamamoto, M. Bartkowiak, N. Kurita, and H. Tanaka, Microscopic evidence of a quantum magnetization process in the $S=1/2$ triangular-lattice Heisenberg-like antiferromagnet $Ba_3CoSb_2O_9$, Phys. Rev. B **100**, 094436 (2019).

[28] E. A. Ghioldi, A. Mezio, L. O. Manuel, R. R. P. Singh, J. Oitmaa, and A. E. Trumper, Magnons and excitation continuum in XXZ triangular antiferromagnetic model: Application to $Ba_3CoSb_2O_9$, Phys. Rev. B **91**, 134423 (2015).

[29] J. Ma, Y. Kamiya, T. Hong, H. B. Cao, G. Ehlers, W. Tian, C. D. Batista, Z. L. Dun, H. D. Zhou, and M. Matsuda, Static and dynamical properties of the spin-1/2 equilateral triangular-lattice antiferromagnet $Ba_3CoSb_2O_9$, Phys. Rev. Lett. **116**, 087201 (2016).

[30] P. A. Maksimov, M. E. Zhitomirsky, and A. L. Chernyshev, Field-induced decays in XXZ triangular-lattice antiferromagnets, Phys. Rev. B **94**, 140407(R) (2016).

[31] S. Ito, N. Kurita, H. Tanaka, S. Ohira-Kawamura, K. Nakajima, S. Itoh, K. Kuwahara, and K. Kakurai, Structure of the magnetic excitations in the spin-1/2 triangular-lattice Heisenberg antiferromagnet $Ba_3CoSb_2O_9$, Nat. Commun. **8**, 235 (2017).

[32] C. Zhang and T. Li, Resonating valence bond theory of anomalous spin dynamics of spin-1/2 triangular lattice Heisenberg antiferromagnet and its application to $Ba_3CoSb_2O_9$, Phys. Rev. B **102**, 075108 (2020).

[33] D. Macdougal, S. Williams, D. Prabhakaran, R. I. Bewley, D. J. Voneshen, and R. Coldea, Avoided quasiparticle decay and enhanced excitation continuum in the spin-$\frac{1}{2}$ near-Heisenberg triangular antiferromagnet $Ba_3CoSb_2O_9$, Phys. Rev. B **102**, 064421 (2020).

[34] R. Chi, Y. Liu, Y. Wan, H.-J. Liao, and T. Xiang, Spin excitation spectra of anisotropic spin-1/2 triangular lattice Heisenberg antiferromagnets, Phys. Rev. Lett. **129**, 227201 (2022).

[35] M. Lee, E. S. Choi, X. Huang, J. Ma, C. R. Dela Cruz, M. Matsuda, W. Tian, Z. L. Dun, S. Dong, and H. D. Zhou, Magnetic phase diagram and multiferroicity of $Ba_3MnNb_2O_9$: A spin-$\frac{5}{2}$ triangular lattice antiferromagnet with weak easy-axis anisotropy, Phys. Rev. B **90**, 224402 (2014).

[36] J. Jiao, S. Zhang, Q. Huang, M. Zhang, M. F. Shu, G. T. Lin, C. R. dela Cruz, V. O. Garlea, N. Butch, M. Matsuda, H. Zhou, and J. Ma, Quantum effect on the ground state of the triple-perovskite $Ba_3MNb_2O_9$ (M = Co, Ni, and Mn) with triangular-lattice, Chem. Mater. **34**, 6617 (2022).

[37] R. Rawl, L. Ge, H. Agrawal, Y. Kamiya, C. R. Dela Cruz, N. P. Butch, X. F. Sun, M. Lee, E. S. Choi, J. Oitmaa, C. D. Batista, M. Mourigal, H. D. Zhou, and J. Ma, $Ba_8CoNb_6O_{24}$: A spin-$\frac{1}{2}$ triangular-lattice Heisenberg antiferromagnet in the two-dimensional limit, Phys. Rev. B **95**, 060412(R) (2017).

[38] R. Rawl, L. Ge, Z. Lu, Z. Evenson, C. R. Dela Cruz, Q. Huang, M. Lee, E. S. Choi, M. Mourigal, H. D. Zhou, and J. Ma, $Ba_8MnNb_6O_{24}$: A model two-dimensional spin-$\frac{5}{2}$ triangular lattice antiferromagnet, Phys. Rev. Mater. **3**, 054412 (2019).

[39] Z. Lu, L. Ge, G. Wang, M. Russina, G. Günther, C. R. dela Cruz, R. Sinclair, H. D. Zhou, and J. Ma, Lattice distortion effects on the frustrated spin-1 triangular-antiferromagnet $A_3NiNb_2O_9$ (A = Ba, Sr, and Ca), Phys. Rev. B **98**, 094412 (2018).

[40] K. Aoyama and H. Kawamura, Spin current as a probe of the $\mathbb{Z}_2$-vortex topological transition in the classical Heisenberg antiferromagnet on the triangular lattice, Phys. Rev. Lett. **124**, 047202 (2020).

[41] K. Tomiyasu, Y. P. Mizuta, M. Matsuura, K. Aoyama, and H. Kawamura, Observation of topological $\mathbb{Z}_2$ vortex fluctuations in the frustrated Heisenberg magnet $NaCrO_2$, Phys. Rev. B **106**, 054407 (2022).

[42] T. Misawa and Y. Motome, Nonequilibrium relaxation study of the anisotropic antiferromagnetic Heisenberg model on the triangular lattice, J. Phys. Soc. Jpn. **79**, 073001 (2010).

[43] Y. P. Mizuta, K. Aoyama, K. Tomiyasu, M. Matsuura, and H. Kawamura, Spin dynamics simulation of the Z_2-vortex fluctuations, J. Phys. Soc. Jpn. **91**, 035001 (2022).

[44] H. Kawamura, A. Yamamoto, and T. Okubo, Z_2-vortex ordering of the triangular-lattice Heisenberg antiferromagnet, J. Phys. Soc. Jpn. **79**, 023701 (2010).

[45] H. Kawamura, Z_2-vortex order of frustrated Heisenberg antiferromagnets in two dimensions, J. Phys.: Conf. Ser. **320**, 012002 (2011).

[46] T. Okubo and H. Kawamura, Signature of a Z_2 vortex in the dynamical correlations of the triangular-lattice Heisenberg antiferromagnet, J. Phys. Soc. Jpn. **79**, 084706 (2010).

[47] B. C. Chakoumakos, H. Cao, F. Ye, A. D. Stoica, M. Popovici, M. Sundaram, W. Zhou, J. S. Hicks, G. W. Lynn, and R. A. Riedel, Four-circle single-crystal neutron diffractometer at the high flux isotope reactor, J. Appl. Cryst. **44**, 655 (2011).

[48] C. Frontera and J. Rodríguez-Carvajal, Fullprof as a new tool for flipping ratio analysis: Further improvements, Phys. B: Condens. Matter **350**, E731 (2004).

[49] Z. M. Tian, C. M. Zhu, Z. W. Ouyang, J. F. Wang, W. Tong, Y. Liu, Z. C. Xia, and S. L. Yuan, Susceptibility, high-field

magnetization and ESR studies in a spin-5/2 triangular-lattice antiferromagnet $Ba_3MnSb_2O_9$, J. Magn. Magne. Mater. **360**, 10 (2014).

[50] Y. C. Sun, Z. W. Ouyang, M. Y. Ruan, Y. M. Guo, J. J. Cheng, Z. M. Tian, Z. C. Xia, and G. H. Rao, High-field magnetization and ESR in the triangular-lattice antiferromagnets $Ba_3MnSb_2O_9$ and $Ba_3TNb_2O_9$ (T=Ni, Co), J. Magn. Magn. Mater. **393**, 273 (2015).

[51] M. F. Collins and O. A. Petrenko, Review/synthèse: Triangular antiferromagnets, Can. J. Phys. **75**, 605 (1997).

[52] H. D. Zhou, C. Xu, A. M. Hallas, H. J. Silverstein, C. R. Wiebe, I. Umegaki, J. Q. Yan, T. P. Murphy, J.-H. Park, Y. Qiu, J. R. D. Copley, J. S. Gardner, and Y. Takano, Successive phase transitions and extended spin-excitation continuum in the $S=\frac{1}{2}$ triangular-lattice antiferromagnet $Ba_3CoSb_2O_9$, Phys. Rev. Lett. **109**, 267206 (2012).

[53] M. Mourigal, W. T. Fuhrman, A. L. Chernyshev, and M. E. Zhitomirsky, Dynamical structure factor of the triangular-lattice antiferromagnet, Phys. Rev. B **88**, 094407 (2013).

[54] J. H. P. Colpa, Diagonalization of the quadratic boson hamiltonian, Physica A **93**, 327 (1978).

[55] G. L. Squires, Magnetic scattering - basic theory, in *Introduction to the Theory of Thermal Neutron Scattering*, 3rd ed. (Cambridge University Press, Cambridge, 2012), pp. 129–145.

[56] M. Oshikawa, New approach to electron spin resonance in quantum spin chains, Prog. Theor. Phys. Suppl. **145**, 243 (2002).

[57] M. Oshikawa and I. Affleck, Electron spin resonance in $s = \frac{1}{2}$ antiferromagnetic chains, Phys. Rev. B **65**, 134410 (2002).

[58] R. Kubo and K. Tomita, A general theory of magnetic resonance absorption, J. Phys. Soc. Jpn. **9**, 888 (1954).

[59] H. Tanaka, T. Ono, S. Maruyama, S. Teraoka, K. Nagata, H. Ohta, S. Okubo, S. Kimura, T. Kambe, H. Nojiri, and M. Motokawa, Electron spin resonance in triangular antiferromagnets, J. Phys. Soc. Jpn. **72**, 84 (2003).

[60] D. Hsieh, D. Qian, R. F. Berger, R. J. Cava, J. W. Lynn, Q. Huang, and M. Z. Hasan, Unconventional spin order in the triangular lattice system $NaCrO_2$: A neutron scattering study, Phys. B: Condens. Matter **403**, 1341 (2008).

[61] S. Nakatsuji, Y. Nambu, H. Tonomura, O. Sakai, S. Jonas, C. Broholm, H. Tsunetsugu, Y. Qiu, and Y. Maeno, Spin disorder on a triangular lattice, Science **309**, 1697 (2005).

[62] S. Nakatsuji, Y. Nambu, and S. Onoda, Novel geometrical frustration effects in the two-dimensional triangular-lattice antiferromagnet $NiGa_2S_4$ and related compounds, J. Phys. Soc. Jpn. **79**, 011003 (2010).

[63] R. M. White, M. Sparks, and I. Ortenburger, Diagonalization of the antiferromagnetic magnon-phonon interaction, Phys. Rev. **139**, A450 (1965).